



ARISTOTLE UNIVERSITY OF THESSALONIKI  
SCHOOL OF ELECTRICAL AND COMPUTER ENGINEERING  
DEPARTMENT OF ELECTRONICS AND COMPUTER ENGINEERING

# **TEXTURAL AND OTHER FEATURES**

APPENDIX OF THE DIPLOMA THESIS  
OF  
NIKOLAOS G. GIAKOUMOGLOU

Supervisor: Anastasios Ntelopoulos

Thessaloniki, July 2021



# **COPYRIGHT**

© Nikolaos Giakoumoglou 2021.

# TABLE OF CONTENTS

|  |          |
|--|----------|
| Copyright .....                          | 3        |
| Table of Contents.....                   | 4        |
| List of Figures .....                    | 5        |
| List of Tables .....                     | 6        |
| <b>Appendices.....</b>                   | <b>7</b> |
| Appendix A. Textural Features .....      | 7        |
| Appendix B. Morphological Features ..... | 28       |
| Appendix C. Histogram Features .....     | 33       |
| Appendix D. Multi-scale Features.....    | 34       |
| Appendix E. Other Features .....         | 40       |

# LIST OF FIGURES

|  |    |
|--|----|
| Figure D-1 Schematic diagram of the (a) 2-D DWT, (b) SWT, and (c) WP decomposition schemes for a given level of analysis. Note that, for $j = 0$ , $A_0$ is the original image, whereas for $j = 1$ , $C_0$ is omitted from the abbreviation of WP sub-images. $H_r$ , $H_c$ , $G_r$ , and $G_c$ are the low-pass and high-pass filters on the rows and columns of each sub-image. The symbols “ $2\downarrow 1$ ” and “ $1\downarrow 2$ ” denote the down-sampling procedure on the columns and rows, respectively, which is valid for DWT and WP only (Tsiaparas, et al., 2011)..... | 35 |
| Figure D-2 DWT decomposition (Lee, et al., 2019).....  | 36 |
| Figure D-3 Multiresolution Feature Extraction: Red sub-image is ignored for analysis (Lee, et al., 2019) .....   | 38 |
| Figure D-4 2-D Multi-scale AM-FM demodulation. Dominant AM-FM components are selected over different image scales. The bandpass filter selector (upper left) is used to define the bandpass filters that correspond to each scale (Murray Herrera, 2009) .....   | 39 |

# LIST OF TABLES

|                                |    |
|--------------------------------|----|
| Table A-1 GLCM notation.....   | 9  |
| Table A-2 NGTDM notation ..... | 13 |
| Table A-3 GLRLM notation ..... | 19 |
| Table A-4 GLSZM notation.....  | 24 |

# Appendices

---

## Appendix A. Textural Features

### A.1. First-order statistics (FOS) or Statistical Features (SF)

Let  $f(x, y)$  be a grayscale image. The first order histogram  $H_i$  is defined as

$$H_i = \frac{\text{number of pixels with gray level } i \text{ inside ROI}}{\text{total number of pixels in the ROI}},$$

which is the empirical probability density function for single pixels. FOS/SF consists of the following parameters:

1. Mean

$$\mu = f_1 = \sum_i i H_i$$

2. Standard Deviation=Variance<sup>1/2</sup>

$$\sigma = f_2 = \sqrt{\sum_i (i - \mu)^2 H_i}$$

3. Median

$$f_3 \text{ s. t. } \sum_{i=0}^{f_3} H_i = 0.5$$

4. Mode

$$f_4 = \operatorname{argmax}_i \{H_i\}$$

5. Skewness

$$f_5 = \sum_i \left( \frac{i - \mu}{\sigma} \right)^3 H_i$$

6. Kurtosis

$$f_6 = \sum_i \left( \frac{i - \mu}{\sigma} \right)^4 H_i$$

7. Energy

$$f_7 = \sum_i H_i^2$$

8. Entropy

$$f_8 = - \sum_i H_i \ln [H_i]$$

9. Minimal Gray Level

$$f_9 = \min \{f(x, y)\}$$

10. Maximal Grey Level

$$f_{10} = \max \{f(x, y)\}$$

11. Coefficient of Variation

$$f_{11} = \frac{\sigma}{\mu}$$

12. 13. 14. 15. Percentiles (10,25,75,90)

$$f_n \text{ s. t. } \sum_{i=0}^{f_n} H_i = c$$

where  $(n, c) = (12, 0.1), (13, 0.25), (14, 0.75), (15, 0.9)$ . Note that 50-Percentile is the median.

16. Histogram Width

$$f_{16} = f_{15} - f_{12}$$

## **A.2. Gray Level Co-occurrence Matrix (GLCM) or Spatial Gray Level Dependence Matrix (SGLDM)**

The Spatial Gray Level Dependence Matrices (SGLDM) as proposed by (Haralick, Shanmugam, & Dinstein, 1973) are based on the estimation of the second-order joint conditional probability density functions,  $\bar{p}(i, j; d, \theta)$ . The  $\bar{p}(i, j; d, \theta)$  is the probability that two pixels  $(k, l)$  and  $(m, n)$  with distance  $d$  in direction specified by the angle  $\theta$  have intensities of gray level  $i$  and gray level  $j$ . The estimated values for these probability density functions will be denoted by  $P(i, j; d, \theta)$ . In a  $N_1 \times N_2$  image, let  $L_1 = \{0, 1, \dots, N_1 - 1\}$  be the horizontal spatial domain,  $L_2 = \{0, 1, \dots, N_2 - 1\}$  be the vertical spatial domain, and  $f(x, y)$  be the image intensity at pixel  $(x, y)$ .



Formally, for angles quantized at  $45^\circ$  intervals, the unnormalized probability density functions are defined by

$$P(i, j; d, 0^\circ) = \#\{((k, l), (m, n)) \in (L_1 \times L_2) \times (L_1 \times L_2): k - m = 0, |l - n| = d, f(k, l) = i, f(m, n) = j\}$$

$$P(i, j; d, 45^\circ) = \#\{((k, l), (m, n)) \in (L_1 \times L_2) \times (L_1 \times L_2): (k - m = d, |l - n| = d) \text{ or } (k - m = -d, l - n = d), f(k, l) = i, f(m, n) = j\}$$

$$P(i, j; d, 90^\circ) = \#\{((k, l), (m, n)) \in (L_1 \times L_2) \times (L_1 \times L_2): |k - m| = d, l - n = 0, f(k, l) = i, f(m, n) = j\}$$

$$P(i, j; d, 135^\circ) = \#\{((k, l), (m, n)) \in (L_1 \times L_2) \times (L_1 \times L_2): (k - m = d, |l - n| = d) \text{ or } (k - m = -d, l - n = -d), f(k, l) = i, f(m, n) = j\}$$

where # denotes the number of elements in the set.

Table A-1 GLCM notation

| <i>Notation</i> | <i>Meaning</i>  |
|-----------------|---|
| $p(i, j)$       | $\frac{P(i, j)}{\sum_{i=0}^{N-1} \sum_{j=0}^{N-1} P(i, j)}$ |
| $N$             | number of gray levels                                       |
| $p_x(i)$        | $\sum_{j=0}^{N-1} p(i, j)$                                  |
| $p_y(j)$        | $\sum_{i=0}^{N-1} p(i, j)$                                  |
| $\mu_x$         | $\sum_{i=0}^{N-1} i p_x(i)$                                 |
| $\mu_y$         | $\sum_{j=0}^{N-1} j p_y(j)$                                 |
| $\sigma_x^2$    | $\sum_{i=0}^{N-1} (i - \mu_x)^2 p_x(i)$                     |

$$\begin{aligned}
\sigma_y^2 &= \sum_{j=0}^{N-1} (j - \mu_y)^2 p_y(j) \\
p_{x+y}(k) &= \sum_{i=0}^{N-1} \sum_{j=0, i+j=k}^{N-1} p(i, j) \\
p_{x-y}(k) &= \sum_{i=0}^{N-1} \sum_{j=0, |i-j|=k}^{N-1} p(i, j) \\
\mu_{x+y} &= \sum_{k=1}^{2N-1} k p_{x+y}(k) \\
\mu_{x-y} &= \sum_{k=0}^{N-1} k p_{x-y}(k)
\end{aligned}$$

The following texture measures that can be extracted from the spatial gray level dependence matrices are proposed in the paper:

1. Angular Second Moment= Energy<sup>2</sup>

$$f_1 = \sum_{i=0}^{N-1} \sum_{j=0}^{N-1} p(i, j)^2$$

2. Contrast

$$f_2 = \sum_{i=0}^{N-1} n^2 \left\{ \sum_{i=0, |i-j|=n}^{N-1} \sum_{j=0}^{N-1} p(i, j) \right\}$$

3. Correlation

$$\begin{aligned}
f_3 &= \sum_{i=0}^{N-1} \sum_{j=0}^{N-1} \left( \frac{i - \mu_x}{\sigma_x} \right) \left( \frac{j - \mu_y}{\sigma_y} \right) p(i, j) = \\
&= \frac{\sum_{i=0}^{N-1} \sum_{j=0}^{N-1} (ij) p(i, j) - \mu_x \mu_y}{\sigma_x \sigma_y}
\end{aligned}$$

4. Sum of Squares: Variance

$$f_4 = \sum_{i=0}^{N-1} \sum_{j=0}^{N-1} (i - \mu)^2 p(i, j)$$

5. Inverse Difference Moment (1<sup>st</sup> formula)/Homogeneity (2<sup>nd</sup> formula)

$$f_5 = \sum_{i=0}^{N-1} \sum_{j=0}^{N-1} \frac{p(i,j)}{1 + (i-j)^2} \text{ or } \sum_{i=0}^{N-1} \sum_{j=0}^{N-1} \frac{p(i,j)}{1 + |i-j|}$$

6. Sum Average

$$f_6 = \sum_{k=1}^{2N-1} kp_{x+y}(k)$$

7. Sum Variance

$$f_7 = \sum_{k=1}^{2N-1} (i - \mu_{x-y})^2 p_{x+y}(k)$$

8. Sum Entropy

$$f_8 = - \sum_{k=1}^{2N-1} p_{x+y}(k) \ln[p_{x+y}(k)]$$

9. Entropy

$$f_9 = - \sum_{i=0}^{N-1} \sum_{j=0}^{N-1} p(i,j) \log[p(i,j)]$$

10. Difference Variance

$$f_{10} = \sum_{k=0}^{N-1} (k - \mu_{x-y})^2 p_{x-y}(k)$$

11. Difference Entropy

$$f_{11} = - \sum_{k=0}^{N-1} p_{x-y}(ik) \log [p_{x-y}(k)]$$

12. 13. Information Measures of Correlation

$$f_{12} = \frac{HXY - HXY1}{\max \{HX, HY\}}$$

$$f_{13} = (1 - \exp(-2.0(HXY2 - HXY)))^{1/2}$$

where

$$HX = - \sum_{i=0}^{N-1} p_x(i) \log[p_x(i)]$$

$$HY = - \sum_{i=0}^{N-1} p_y(i) \log[p_y(i)]$$

$$\begin{aligned}
HXY &= \sum_{i=0}^{N-1} \sum_{j=0}^{N-1} p(i,j) \log[p(i,j)] \\
HXY1 &= - \sum_{i=0}^{N-1} \sum_{j=0}^{N-1} p(i,j) \log[p_x(i,j) P p_y(i,j)] \\
HXY2 &= - \sum_{i=0}^{N-1} \sum_{j=0}^{N-1} p(i,j) \log[p_x(i,j) P p_y(i,j)]
\end{aligned}$$

#### 14. Maximal Correlation Coefficient

$$f_{14} = (\text{Second largest Eigenvalue of } Q)^{1/2}$$

where

$$Q(i,j) = \sum_{k=0}^{N-1} \frac{p(i,k)p(j,k)}{p_x(i)p_y(k)}$$

For a chosen distance  $d$  we have four angular SGLDM. Hence, we obtain a set of four values for each of the preceding measures. The mean and range of each of these measures, averaged over the four values, comprise the set of features.

### A.3. Gray Level Difference Statistics (GLDS)

The Gray Level Difference Statistics (GLDS) algorithm (Weszka, Dyer, & Rosenfeld, 1976) uses first order statistics of local property values based on absolute differences between pairs of gray levels or of average gray levels in order to extract texture measures. Let  $f(x, y)$  be the image intensity function and for any given displacement  $\delta = (\Delta x, \Delta y)$ , let  $f_\delta(x, y) = |f(x, y) - f(x + \Delta x, y + \Delta y)|$ . Let  $p_\delta$  be the probability density of  $f_\delta(x, y)$ . If there are  $N$  gray levels, this has the form of an  $N$ -dimensional vector whose  $i^{\text{th}}$  component is the probability that  $f_\delta(x, y)$  will have value  $i$ . The probability density  $p_\delta$  can be easily computed by counting the number of times each value of  $f_\delta(x, y)$  occurs, where  $\Delta x$  and  $\Delta y$  are integers. In a coarse texture, if the  $d$  is small,  $f_\delta(x, y)$  will be small, i.e., the values of  $p_\delta$  should be concentrated near  $i = 0$ . Conversely, in a fine texture, the values of  $p_\delta$  should be more spread out. Thus, a good way to analyse texture coarseness would be to compute, for various magnitudes of  $\delta$ , some measure of the spread of values in  $p_\delta$  away from the origin. Such measures are the following:

#### 1. Homogeneity

$$f_1 = \sum_i \frac{p_\delta(i)}{i^2 + 1}$$

2. Contrast

$$f_2 = \sum_i i^2 p_\delta(i)$$

3. Energy/ Angular Second Moment

$$f_3 = \sum_i p_\delta(i)^2$$

4. Entropy

$$f_4 = - \sum_i p_\delta(i) \log[p_\delta(i)]$$

5. Mean

$$f_5 = \sum_i i p_\delta(i)$$

#### A.4. Neighbourhood Gray Tone Difference Matrix (NGTDM) method

Neighbourhood Gray Tone Difference Matrix (NDTDM) (Amadasun & King, 1989) corresponds to visual properties of texture. Let  $f(x, y)$  be the gray tone of a pixel at  $(x, y)$  having gray tone value  $i$ . Then the average gray tone over a neighborhood centered at, but excluding  $(x, y)$ , can be found

$$A_i = A(x, y) = \frac{1}{W - 1} \sum_{x'=-d}^d \sum_{y'=-d}^d f(x + x', y + y')$$

where  $(x', y') \neq (0, 0)$ ,  $d$  specifies the neighbourhood size and  $W = (2d + 1)^2$ . Then the  $i^{\text{th}}$  entry in the NGTDM is

$$s(i) = \begin{cases} \sum |i - A_i|, & \text{for } i \in N_i \text{ if } N_i \neq 0 \\ 0, & \text{otherwise} \end{cases}$$

where  $\{N_i\}$  is the set of all pixels having gray tone  $i$ .

Table A-2 NGTDM notation

| <i>Notation</i> | <i>Meaning</i>                               |
|-----------------|--|
| $G_h$           | highest gray tone value present in the image |

|                         |   |
|-------------------------|---|
| $\varepsilon$           | a small number  |
| $p_i = \frac{N_i}{n^2}$ | the probability of occurrence of gray tone value $i$ in a $N \times N$ image where $n = N - 2d$ |
| $N_g$                   | total number of different gray levels present in the image                                      |

The following textural features are defined as

1. Coarseness

$$f_1 = \left[ \varepsilon + \sum_{i=0}^{G_h} p_i s(i) \right]^{-1}$$

2. Contrast

$$f_2 = \left[ \frac{1}{N_g(N_g - 1)} \sum_{i=0}^{G_h} \sum_{j=0}^{G_h} p_i p_j (i - j)^2 \right] \left[ \frac{1}{n^2} \sum_{i=0}^{G_h} s(i) \right]$$

3. Busyness

$$f_3 = \frac{[\sum_{i=0}^{G_h} p_i s(i)]}{[\sum_{i=0}^{G_h} i p_i - j p_j]}, p_i \neq 0, p_j \neq 0$$

4. Complexity

$$f_4 = \sum_{i=0}^{G_h} \sum_{j=0}^{G_h} \{(|i - j|)/(n^2(p_i + p_j))\} \{p_i s(i) + p_j s(j)\}$$

$$p_i \neq 0, p_j \neq 0$$

5. Strength

$$f_5 = \left[ \sum_{i=0}^{G_h} \sum_{j=0}^{G_h} (p_i + p_j)(i - j)^2 \right] / \left[ \varepsilon + \sum_{i=0}^{G_h} s(i) \right], p_i \neq 0, p_j \neq 0$$

#### A.5. Statistical Feature Matrix (SFM)

The Statistical Feature Matrix (Wu & Chen, Statistical feature matrix for texture analysis, 1992) measures the statistical properties of pixel pairs at several distances within an image which are used for statistical analysis. Let  $f(x, y)$  be the intensity at point  $(x, y)$ , and let  $\delta = (\Delta x, \Delta y)$  represent the intersample spacing distance vector, where  $\Delta x$  and  $\Delta y$  are integers. The  $\delta$  contrast,  $\delta$  covariance, and  $\delta$  dissimilarity are defined as

$$CON(\delta) = E\{|f(x, y) - f(x + \Delta x, y + \Delta y)|^2\}$$

$$COV(\delta) = E\{[f(x, y) - \eta][f(x + \Delta x, y + \Delta y) - \eta]\}$$

$$DSS(\delta) = E\{|f(x, y) - f(x + \Delta x, y + \Delta y)|\}$$

where  $E\{\}$  denotes the expectation operation and  $\eta$  is the average gray level of the image. A statistical feature matrix, (SFM)  $M_{sf}$ , is an  $(L_r + 1) \times (2L_c + 1)$  matrix whose  $(i, j)$  element is the  $\delta$  statistical feature of the image, where  $\delta = (j - L_c, i)$  is an intersample spacing distance vector for  $i = 0, 1, \dots, L_r$ ,  $j = 0, 1, \dots, L_c$ , and  $L_r, L_c$  are the constants which determine the maximum intersample spacing distance. In a similar way, the contrast matrix ( $M_{con}$ ), covariance matrix ( $M_{cov}$ ), and dissimilarity matrix ( $M_{dss}$ ) can be defined as the matrices whose  $(i, j)$  elements are the  $\delta$  contrast,  $\delta$  covariance, and  $\delta$  dissimilarity, respectively. Based on the SFM, the following texture features can be computed:

1. Coarseness

$$f_1 = \frac{c}{\sum_{(i,j) \in N_r} \frac{DSS(i,j)}{n}}$$

where  $c$  is a normalized factor,  $N_r$  is the set of displacement vectors defined as  $N_r = \{(i, j): |i|, |j| < r\}$  and  $n$  is the number of elements in the set.

2. Contrast

$$f_2 = \left[ \sum_{(i,j) \in N_r} \frac{CON(i,j)}{4} \right]^{1/2}$$

3. Periodicity

$$f_3 = \frac{\bar{M}_{dss} - M_{dss}(valley)}{\bar{M}_{dss}}$$

where  $\bar{M}_{dss}$  is the mean of all elements in  $M_{dss}$  and  $M_{dss}(valley)$  is the deepest valley in the matrix

4. Roughness

$$f_4 = \frac{D_f^{(h)} + D_f^{(v)}}{2}$$

where  $D_f$  is the fractal dimension (see Fractal Dimension Texture Analysis (FDTA)) in horizontal and vertical dimensions.  $D_f = 3 - H$  and  $E\{-\Delta I\} = k(\delta)^H$  where  $H$  can be estimated from the dissimilarity matrix since the  $(i, j + L_c)$  element of the matrix is  $E\{-\Delta I\}$  with  $\delta = (j, i)$ .

#### A.6. Law's Texture Energy (LTE) Method (TEM)

Law's texture Energy Measures (Laws, 1980), (Wu, Chen, & Hsieh, Texture features for classification of ultrasonic liver images, 1992) are derived from three simple vectors of length 3,  $L3 = (1, 2, 1)$ ,  $E3 = (-1, 0, 1)$ , and  $S3 = (-1, 2, -1)$ , which represent the one-dimensional operations of center-weighted local averaging, symmetric first differencing for edge detection, and second differencing for spot detection. If these vectors are convolved with themselves, new vectors of length 5,  $L5 = (1, 4, 6, 4, 1)$ ,  $E5 = (-1, -2, 0, 2, 1)$  and  $S5 = (-1, 0, 2, 0, -1)$  are obtained. By further self-convolution, new vectors of length 7,  $L7 = (1, 6, 15, 20, 15, 6, 1)$ ,  $E7 = (-1, -4, -5, 0, 5, 4, 1)$  and  $S7 = (-1, -2, 1, 4, 1, 1, -2, -1)$  are obtained, where  $L7$  again performs local averaging,  $E7$  acts as edge detector, and  $S7$  acts as spot detector. If the column vectors of length  $l$  are multiplied by row vectors of the same length, Laws  $l \times l$  masks are obtained. The following combinations are used to obtain the masks (for  $l = 7$ ):

$$LL = L7^T L7$$

$$LE = L7^T E7$$

$$LS = L7^T S7$$

$$EL = E7^T L7$$

$$EE = E7^T E7$$

$$ES = E7^T S7$$

$$SL = S7^T L7$$

$$SE = S7^T E7$$

$$SS = S7^T S7$$



In order to extract texture features from an image, these masks are convoluted with the image, and the statistics (e.g., energy) of the resulting image are used to describe texture. The following texture features were extracted:

1. LL- texture energy from LL kernel
2. EE- texture energy from EE kernel
3. SS- texture energy from SS kernel
4. LE- average texture energy from LE and EL kernels  $LE = (LE + EL)/2$
5. ES- average texture energy from ES and SE kernels  $ES = (ES + SE)/2$
6. LS- average texture energy from LS and SL kernels  $LS = (LS + SL)/2$

The averaging of matched pairs of energy measures gives rotational invariance.

#### **A.7. Fractal Dimension Texture Analysis (FDTA)**

Fractal Dimension Texture Analysis (FDTA) (Wu, Chen, & Hsieh, Texture features for classification of ultrasonic liver images, 1992) is based on the Fractional Brownian Motion (FBM) Model (Mandelbrot, 1977). The FBM model is used to describe the roughness of nature surfaces. It regards naturally occurring surfaces as the end result of random walks. Such random walks are basic physical processes in our universe. An intensity surface of an ultrasonic image can also be viewed as the end result of a random walk, so the FBM model can be suitable for the analysis of ultrasonic liver images.

One of the most important parameters to represent a fractal surface is the fractal dimension. Theoretically, the fractal dimension  $D_f$  is estimated from the equation

$$E(\Delta I^2) = c(\Delta r)^{6-2D_f}$$

where  $E(\cdot)$  denotes the expectation operator,  $\Delta I = I(x_2, y_2) - I(x_1, y_1)$  is the intensity variations between two pixels,  $c$  is a constant, and  $\Delta r = ||(x_2, y_2) - (x_1, y_1)||$  is the spatial distance. A simpler method is to estimate the  $H$  parameter (Hurst coefficient) from the relationship

$$E(|\Delta I|) = k(\Delta r)^H$$

where  $k = E(|\Delta I|)_{\Delta r=1}$ . By applying the  $\log$  function the following is obtained

$$\log E(|\Delta I|) = \log k + H \cdot \log(\Delta r)$$

From the above equation, we can deduce a procedure to estimate the  $H$  parameter and the fractal dimension can be easily computed from the relationship

$$D_f = 3 - H$$

A small value of fractal dimension  $D_f$  (large value of parameter  $H$ ) means a smooth surface, and large  $D$  (small  $H$ ), a rough surface.

Given an  $M \times M$  image, the intensity difference vector is defined as

$$IDV = [id(1), id(2), \dots, id(s)]$$

where  $s$  is the maximum possible scale,  $id(k)$  is the average of the absolute intensity difference of all pixel pairs with vertical or horizontal distance  $k$  and

$$id(k) = \frac{\sum_{x=0}^{M-1} \sum_{y=0}^{M-k-1} |f(x, y) - f(x, y + k)| + \sum_{x=0}^{M-k-1} \sum_{y=0}^{M-1} |f(x, y) - f(x + k, y)|}{2M(M - k - 1)}$$

The value of the parameter  $H$  can be obtained by using least squares linear regression to estimate the slope of the curve of  $id(k)$  versus  $k$  in log-log scales.

If the image is seen under different resolutions, then the multiresolution fractal ( $MF$ ) feature vector is defined as

$$MF = (H^m, H^{m-1}, \dots, H^{m-n+1})$$

where  $M = 2^m$  is the size of the original image,  $H^k$  is the  $H$  parameter estimated from image  $I^k$ , and  $n$  is the number of resolutions chosen. The multiresolution fractal ( $MF$ ) feature vector describes also the lacunarity of the image. It can be used for the separation of textures with the same fractal dimension  $D_f$  by considering all but the first components of the  $MF$  vectors.

### A.8. Gray Level Run Length Matrix (GLRLM)

A gray level run is a set of consecutive, collinear picture points having the same gray level value. The length of the run is the number of picture points in the run (Galloway, 1975). For a given picture, we can compute a gray level run length matrix for runs having any given direction  $\theta$ . Often the direction  $\theta$  is set as  $0, 45, 90, 135^\circ$ . The matrix element  $p_\theta(i, j)$  specifies the number of times that the picture contains a run of length  $j$ , in the given direction, consisting of points having gray level  $i$  (or lying in gray level range  $i$ ). Computation of these matrices is very simple. The number of calculations is directly proportional to the number of points in the picture. Also, the

entire picture need not reside in core. Only two rows of picture values are needed at any one time to compute the matrices. To obtain numerical texture measures from the matrices, we can compute functions analogous to those used by Haralick for gray level co-occurrence matrices.

Table A-3 GLRLM notation

| <i>Notation</i>    | <i>Meaning</i>   |
|--------------------|--|
| $p_{\theta}(i, j)$ | The $(i, j)^{\text{th}}$ entry in the given run length matrix for direction $\theta$ |
| $N_g$              | Number of gray levels in the image   |
| $N_r$              | Number of different run length that occur (so the matrix is $N_g \times N_r$ )       |
| $N_z$              | $\sum_{i=1}^{N_g} \sum_{j=1}^{N_r} p_{\theta}(i, j)$                                 |
| $N_p$              | The number of voxels in the image  |

The RUNL features are the following:

1. Short Run Emphasis

$$f_1 = \frac{\sum_{i=0}^{N_g-1} \sum_{j=0}^{N_r-1} \frac{p_{\theta}(i, j)}{j^2}}{N_z}$$

2. Long Run Emphasis

$$f_2 = \frac{\sum_{i=0}^{N_g-1} \sum_{j=0}^{N_r-1} j^2 p_{\theta}(i, j)}{N_z}$$

3. Gray Level Non-Uniformity/Gray Level Distribution

$$f_3 = \frac{\sum_{i=0}^{N_g-1} \left( \sum_{j=0}^{N_r-1} p_{\theta}(i, j) \right)^2}{N_z}$$

4. Run Length Non-Uniformity/Run Length Distribution

$$f_4 = \frac{\sum_{j=0}^{N_r-1} \left( \sum_{i=0}^{N_g-1} p_{\theta}(i, j) \right)^2}{N_z}$$

5. Run Percentage

$$f_5 = \frac{N_z}{N_p}$$

6. Low Gray Level Run Emphasis

$$f_6 = \frac{\sum_{i=0}^{N_g-1} \sum_{j=0}^{N_r-1} \frac{p_\theta(i,j)}{i^2}}{N_z}$$

7. High Gray Level Run Emphasis

$$f_7 = \frac{\sum_{i=0}^{N_g-1} \sum_{j=0}^{N_r-1} p_\theta(i,j) i^2}{N_z}$$

8. Short Low Gray Level Emphasis

$$f_8 = \frac{\sum_{i=0}^{N_g-1} \sum_{j=0}^{N_r-1} \frac{p_\theta(i,j)}{i^2 j^2}}{N_z}$$

9. Short Run High Gray Level Emphasis

$$f_9 = \frac{\sum_{i=0}^{N_g-1} \sum_{j=0}^{N_r-1} \frac{p_\theta(i,j)}{j^2}}{N_z}$$

10. Long Run Low Gray Level Emphasis

$$f_{10} = \frac{\sum_{i=0}^{N_g-1} \sum_{j=0}^{N_r-1} \frac{p_\theta(i,j)}{i^2}}{N_z}$$

11. Long Run High Gray Level Emphasis

$$f_{11} = \frac{\sum_{i=1}^{N_g-1} \sum_{j=1}^{N_r-1} p_\theta(i,j) i^2 j^2}{N_z}$$

### A.9. Fourier Power Spectrum (FPS)

The Fourier transform (Weszka, Dyer, & Rosenfeld, 1976), (Wu, Chen, & Hsieh, Texture features for classification of ultrasonic liver images, 1992) of a picture  $f(x, y)$  is defined by

$$F(u, v) = \int_{-\infty}^{\infty} \int_{-\infty}^{\infty} e^{-2\pi i(ux+vy)} f(x, y) dx dy$$

and the Fourier power spectrum, is  $|F|^2 = FF^*$  (where  $*$  denotes the complex conjugate).

It is well known that the radial distribution of values in  $|F|^2$  is sensitive to texture coarseness in  $f$ . A coarse texture will have high values of  $|F|^2$  concentrated near the origin while in a fine texture the values of  $|F|^2$  will be more spread out. Thus, if one wishes to analyse texture coarseness, a set of features that should be useful are the averages of  $|F|^2$  taken over a ring-shaped regions centred at the origin i.e. features of the form

$$\varphi_r = \int_0^{2\pi} |F(r, \theta)|^2 d\theta$$

for various values of  $r$ , the ring radius.

Similarly, it is well known that the angular distribution of values in  $|F|^2$  is sensitive to the directionality of the texture in  $f$ . A texture with many edges or lines in a given direction  $\theta$  will have high values of  $|F|^2$  concentrated around the perpendicular direction  $\theta + (\frac{\pi}{2})$ , while in a nondirectional texture,  $|F|^2$  should also be nondirectional. Thus, a good set of features for analysing texture directionality should be the averages of  $|F|^2$  taken over a wedge-shaped regions entered at the origin, i.e., features of the form

$$\varphi_\theta = \int_0^\infty |F(r, \theta)|^2 dr$$

for various values of  $\theta$ , the wedge slope.

For  $N \times N$  digital pictures, instead of the continuous Fourier transform defined above, one uses the discrete transform defined by

$$F(u, v) = \frac{1}{N^2} \sum_{i,j=0}^{N-1} f(i, j) e^{-2\pi\sqrt{-1}(iu+jv)}$$

where  $0 \leq u$  and  $v \leq N - 1$ . This transform, however treats the input picture  $f(x, y)$  as periodic. If, in fact, it is not, the transform is affected by the discontinuities that exist between one edge of  $f$  and the opposite edge. These have the effect of introducing

spurious horizontal and vertical directionalities, so that high values are present in  $|F|^2$  along the  $u$  and  $v$  axes.

The standard set of texture features based on a ring-shaped samples of the discrete Fourier power spectrum are of the form

$$\varphi_{r_1, r_2} = \sum_{r_1 \leq u^2 + v^2 \leq r_2} |F(u, v)|^2$$

for various values of the inner and outer ring radii  $r_1$  and  $r_2$ . Similarly, the features based on a wedge-shaped samples are of the form

$$\varphi_{\theta_1, \theta_2} = \sum_{\theta_1 \leq \tan^{-1}\left(\frac{v}{u}\right) \leq \theta_2} |F(u, v)|^2$$

Note that in this last set of features, the “DC value”  $(u, v) = (0, 0)$  has been omitted, since it is common to all the wedges.

#### **A.10. Shape parameters**

Shape parameters consists of the following parameters:

1. X-coordinate maximum length
2. Y-coordinate maximum length
3. area
4. perimeter
5.  $\text{perimeter}^2/\text{area}$

#### **A.11. High Order Spectra (HOS) on Radon Transform**

Radon transform (Chua, Chandran, Acharya, & Lim, Application of Higher Order Spectra to Identify Epileptic EEG, 2011), (Chua, Chandran, Acharya, & Lim, Automatic identification of epileptic electroencephalography signals using higher-order spectra, 2009) transforms two dimensional images with lines into a domain of possible line parameters, where each line in the image will give a peak positioned at the corresponding line parameters. Hence, the lines of the images are transformed into the points in the Radon domain. An equation of the line can be expressed as:  $\rho = x \cdot \cos\theta + y \cdot \sin\theta$ , where  $\theta$  is the small angle and  $\rho$  is the small distance to the origin of the coordinate system. Given a function  $f(x, y)$ , Radon transform is defined as:

$$R(\rho, \theta) = \int_{-\infty}^{\infty} f(\rho \cdot \cos\theta - s \cdot \sin\theta, \rho \cdot \sin\theta + s \cdot \cos\theta) ds$$

This equation describes the integral along a line  $s$  through the image, where  $\rho$  is the distance of the line from the origin and  $\theta$  is the angle from the horizontal. So, radon transform converts 2D signal into the 1D parallel beam projections, at various angles,  $\theta$ .

High Order Spectra (HOS) are spectral components of higher moments. The bispectrum  $B(f_1, f_2)$ , of a signal is the Fourier transform (FT) of the third order correlation of the signal (also known as the third order cumulant function). It is given by

$$B(f_1, f_2) = E\{X(f_1)X(f_2)X^*(f_1 + f_2)\}$$

where  $X(f)$  is the FT of the signal  $x[n]$ ,  $E[\cdot]$  stands for the expectation operation and  $X^*(f_1 + f_2)$  denotes the complex conjugate of  $X(f_1 + f_2)$ . The frequency  $f$  may be normalized by the Nyquist frequency to be between 0 and 1. The bispectrum, is a complex-valued function of two frequencies. The bispectrum which is the product of three Fourier coefficients, exhibits symmetry and was computed in the non-redundant region. This is termed as  $\Omega$ , the principal domain or the nonredundant region.

The extracted feature is (Acharya, Chua, Lim, Tay, & Suri, 2009), (Acharya U, Chua, Ng, Yu, & Chee, 2008) the entropy 1 ( $P_1$ )

$$Entropy1: P_1 = - \sum_i p_i \log(p_i)$$

where

$$p_i = \frac{|B(f_1, f_2)|}{\sum_{\Omega} |B(f_1, f_2)|}$$

#### **A.12. Local Binary Pattern (LPB)**

Local Binary Pattern (LBP), a robust and efficient texture descriptor, was first presented by (Ojala, Pietikäinen, & Harwood, 1996) and (Ojala, Pietikäinen, & Maenpaa, Multiresolution Gray-Scale and Rotation Invariant Texture Classification with Local Binary Patterns, 2002). The LBP feature vector, in its simplest form, is determined using the following method: A circular neighbourhood is considered around a pixel.  $P$  points are chosen on the circumference of the circle with radius  $R$

such that they are all equidistant from the center pixel. Let  $g_c$  be the gray value of the centre pixel and  $g_p, p = 0, \dots, P - 1$ , corresponds to the gray values of the  $P$  points. These  $P$  points are converted into a circular bit-stream of 0s and 1s according to whether the gray value of the pixel is less than or greater than the gray value of the centre pixel. Ojala et al. (2002) introduced the concept of uniformity in texture analysis. The uniform fundamental patterns have a uniform circular structure that contains very few spatial transitions  $U$  (number of spatial bitwise 0/1 transitions). In this work, a rotation invariant measure called  $LBP_{P,R}$  using uniformity measure  $U$  was calculated. Only patterns with  $U \leq 2$  were assigned the LBP code i.e., if the number of bittransitions in the circular bit-stream is less than or equal to 2, the centre pixel was labelled as uniform.

$$LBP_{P,R}(x) = \begin{cases} \sum_{p=0}^{P-1} s(g_p - g_c), & \text{if } U(x) \leq 2 \\ P + 1, & \text{otherwise} \end{cases}$$

where

$$s(x) = \begin{cases} x, & x \geq 0 \\ 0, & x < 0 \end{cases}$$

Multiscale analysis of the image using LBP is done by choosing circles with various radii around the centre pixels and, thus, constructing separate LBP image for each scale. Energy and entropy of the LBP image, constructed over different scales ( $R = 1, 2, 3$  with corresponding pixel count  $P = 8, 16, 24$  respectively) were used as feature descriptors.

### A.13. Gray Level Size Zone Matrix (GLSZM)

Gray Level Size Zone Matrix (GLSZM) (Thibault, et al., 2009) quantifies gray level zones in an image. A gray level zone is defined as the number of connected voxels that share the same gray level intensity. A voxel is considered connected if the distance is 1 according to the infinity norm (26-connected region in a 3D, 8-connected region in 2D). In a gray level size zone matrix  $P(i, j)$  the  $(i, j)$ th element equals the number of zones with gray level  $i$  and size  $j$  appear in image. Contrary to GLCM and GLRLM, the GLSZM is rotation independent, with only one matrix calculated for all directions in the ROI.

Table A-4 GLSZM notation



| <i>Notation</i>                                      | <i>Meaning</i>   |
|--|--|
| $N_g$  | Number of discrete intensity values                    |
| $N_s$  | Number of discrete zones                               |
| $N_p$  | Number of voxels                                       |
| $N_z = \sum_{i=0}^{N_g-1} \sum_{j=0}^{N_s-1} P(i,j)$ | Number of zones in the ROI where $1 \leq N_z \leq N_p$ |
| $P(i,j)$   | Size zone matrix                                       |
| $p(i,j) = \frac{P(i,j)}{N_z}$                        | Normalized size zone matrix                            |

The following features can be calculated

1. Small Zone Emphasis (SZE) or Small Area Emphasis (SAE)

$$f_1 = \sum_{i=0}^{N_g-1} \sum_{j=0}^{N_s-1} \frac{p(i,j)}{j^2}$$

2. Large Zone Emphasis (LZE) or Large Area Emphasis (LAE)

$$f_2 = \sum_{i=0}^{N_g-1} \sum_{j=0}^{N_s-1} p(i,j)j^2$$

3. Gray-Level Non-Uniformity (GLN)

$$f_3 = \frac{\sum_{i=0}^{N_g-1} \left( \sum_{j=0}^{N_s-1} P(i,j) \right)^2}{N_z} \text{ or } \frac{\sum_{i=0}^{N_g-1} \left( \sum_{j=0}^{N_s-1} P(i,j) \right)^2}{N_z^2}$$

4. Zone-Size Non-Uniformity (ZSN)

$$f_4 = \frac{\sum_{j=0}^{N_s-1} \left( \sum_{i=0}^{N_g-1} P(i,j) \right)^2}{N_z} \text{ or } \frac{\sum_{j=0}^{N_s-1} \left( \sum_{i=0}^{N_g-1} P(i,j) \right)^2}{N_z^2}$$

5. Zone Percentage (ZP)

$$f_5 = \frac{N_z}{N_p}$$

6. Low Gray-Level Zone Emphasis (LGLZE)

$$f_6 = \sum_{i=0}^{N_g-1} \sum_{j=0}^{N_s-1} \frac{p(i,j)}{i^2}$$

7. High Gray-Level Zone Emphasis (HGLZE)

$$f_7 = \sum_{i=0}^{N_g-1} \sum_{j=0}^{N_s-1} p(i,j) i^2$$

8. Small Zone Low Gray-Level Emphasis (SZLGLE) or Small Area Low Gray-Level Emphasis (SALGLE)

$$f_8 = \sum_{i=0}^{N_g-1} \sum_{j=0}^{N_s-1} \frac{p(i,j)}{i^2 j^2}$$

9. Small Zone High Gray-Level Emphasis (SZHGLE) or Small Area High Gray-Level Emphasis (SAHGLE)

$$f_9 = \sum_{i=0}^{N_g-1} \sum_{j=0}^{N_s-1} \frac{p(i,j) i^2}{j^2}$$

10. Large Zone Low Gray-Level Emphasis (LZLGLE) or Large Area Low Gray-Level Emphasis (LALGLE)

$$f_{10} = \sum_{i=0}^{N_g-1} \sum_{j=0}^{N_s-1} \frac{p(i,j) j^2}{i^2}$$

11. Large Zone High Gray-Level Emphasis (LZHGLE) or Large Area High Gray Level Emphasis (LAHGLE)

$$f_{11} = \sum_{i=0}^{N_g-1} \sum_{j=0}^{N_s-1} p(i,j) i^2 j^2$$

12. Gray-Level Variance (GLV)

$$f_{12} = \sum_{i=0}^{N_g-1} \sum_{j=0}^{N_s-1} p(i,j) (i - \mu)^2$$

$$\mu = \sum_{i=0}^{N_g-1} \sum_{j=0}^{N_s-1} p(i,j) i$$

### 13. Zone-Size Variance (ZSV)

$$f_{13} = \sum_{i=0}^{N_g-1} \sum_{j=0}^{N_s-1} p(i,j)(j - \mu)^2$$

$$\mu = \sum_{i=0}^{N_g-1} \sum_{j=0}^{N_s-1} p(i,j)j$$

### 14. Zone-Size Entropy (ZSE)

$$f_{14} = - \sum_{i=0}^{N_g-1} \sum_{j=0}^{N_s-1} p(i,j) \log_2(p(i,j) + \varepsilon)$$

$\varepsilon$  is an arbitrarily small positive number

## Appendix B. Morphological Features

### B.1. Multilevel Binary Morphological Analysis

In multilevel binary morphological analysis (Maragos, Pattern spectrum and multiscale shape representation. IEEE Trans Pattern Anal Mach Intell, 1989), (Maragos & Ziff, Threshold Superposition in Morphological Image Analysis Systems., 1990), (Toet, 1990), different plaque components are extracted and investigated for their geometric properties. Three binary images are generated by thresholding.

$$L = \{(x, y) \text{ s. t. } f(x, y) < 25\}$$

$$M = \{(x, y) \text{ s. t. } 25 \leq f(x, y) \leq 50\}$$

$$H = \{(x, y) \text{ s. t. } f(x, y) > 50\}$$

Here, binary image outputs are represented as sets of image coordinates where image intensity meets the threshold criteria. Overall, this multilevel decomposition is closely related to a three-level quantization of the original image intensity. In  $L$ , dark image regions representing blood, thrombus, lipid, or haemorrhage are extracted. Similarly, in  $H$ , collagen and calcified components of the plaque are extracted, while in  $M$ , image components that fall between the two are extracted. In the following discussion, the symbol  $X$  will be used to denote any one of the three binary images  $L, M, H$ .

The structural element, also known as pattern or kernel is defined as the set

$$B = \{(-1,0), (0,0), (1,0), (0,-1), (0,1)\} \subseteq Z^2$$

The two basic operators in the area of mathematical morphology are erosion and dilation. The basic effect of the erosion on a binary image is to erode the boundaries of regions of foreground pixels (i.e., white pixels, typically). Thus, areas of foreground pixels shrink in size, and holes within those areas become larger. Erosion is defined as

$$X \ominus B = \bigcup_{p \in B} X - p = \{a: B + a \subseteq X\}$$

The basic effect of the dilation on a binary image is to gradually enlarge the boundaries of regions of foreground pixels (i.e., white pixels, typically). Thus areas of

foreground pixels grow in size while holes within those regions become smaller. Dilation is defined as

$$X \oplus B = \bigcup_{p \in B} X + p = \{a + b: a \in X \text{ and } b \in B\}$$

The  $n$ -fold expansion of  $B$  also known as  $n$ -fold Minkowski addition of  $B$  with itself is defined as

$$nB = \begin{cases} \{(0,0)\}, n = 0 \\ \underbrace{B \oplus B \oplus \dots \oplus B}_{n-1 \text{ dilations}}, n > 1 \end{cases}$$

Opening and closing are two important operators from mathematical morphology. They are both derived from the fundamental operations of erosion and dilation. The basic effect of an opening is somewhat like erosion in that it tends to remove some of the foreground (bright) pixels from the edges of regions of foreground pixels. However, it is less destructive than erosion in general. The effect of the opening is to preserve foreground regions that have a similar shape to this structuring element, or that can completely contain the structuring element, while eliminating all other regions of foreground pixels. Opening is defined as an erosion followed by a dilation:

$$X \circ B = (X \ominus B) \oplus B$$

Closing is similar in some ways to dilation in that it tends to enlarge the boundaries of foreground (bright) regions in an image (and shrink background colour holes in such regions), but it is less destructive of the original boundary shape. The effect of the closing is to preserve background regions that have a similar shape to this structuring element, or that can completely contain the structuring element, while eliminating all other regions of background pixels. Closing is defined as a dilation followed by an erosion:

$$X \bullet B = (X \oplus B) \ominus B$$

Opening and closing are idempotent, i.e., their successive applications do not change further the previously transformed result

$$X \circ B = (X \circ B) \circ B$$

$$X \bullet B = (X \bullet B) \bullet B$$

We define as a multiscale opening of  $X$  by  $B$  also known as set-processing (SP) opening at scale  $n = 0, 1, 2, \dots$ , the opening

$$X \circ nB = (X \ominus nB) \oplus nB$$

A dual multiscale filter is the closing of  $X$  by  $nB$  or set-processing (SP) closing

$$X \bullet nB = (X \oplus nB) \ominus nB$$

The SP opening can be implemented more efficiently as

$$X \circ nB = \left[ \underbrace{(X \ominus B) \ominus B \ominus \dots \ominus B}_{n \text{ times}} \right] \left[ \underbrace{\oplus B \oplus B \oplus \dots \oplus B}_{n \text{ times}} \right]$$

The set difference images can be formed as

$$d_0(X; B) = X - X \circ B$$

$$d_1(X; B) = X \circ B - X \circ 2B$$

...

$$d_{n-1}(X; B) = X \circ (n-1)B - X \circ nB$$

The pattern spectrum is defined as the function

$$PS_X(n, B) = A[X \circ nB] - A[X \circ (n+1)B] = A[d_n(X; B)], \quad n \geq 0$$

hence the discrete pattern spectrum can be obtained via a forward area difference. A probability density function (pdf) measure is considered defined as

$$pdf_X(n, B) = \frac{A(PS_X(n, B))}{A(X)}, \text{ for } n > 0$$

Given the pdf-measure, the cumulative distribution function (cdf) can also be constructed using

$$cdf_X(n, B) = \begin{cases} 0, & n = 0 \\ \sum_{r=0}^{n-1} pdf_X(r, B), & r+1 \geq n > 0 \end{cases}$$

## B.2. Gray Scale Morphological Analysis

Similarly, we henceforth represent graytone images by functions; filters whose inputs and outputs are functions (multilevel signals) are called function-processing (FP) filters. Let  $f(x, y)$  be a finite support graytone image function on  $Z^2$ , and let  $g(x, y)$  be a fixed graytone pattern. In the context of morphology,  $g$  is called function structuring element.

The mathematical definition for grayscale erosion and dilation is identical except in the way in which the set of coordinates associated with the input image is derived. The erosion and the dilation of  $f$  by  $g$  are respectively the functions

$$(f \ominus g)(x, y) = \min_{(i,j)} \{f(x + i, y + j) - g(i, j)\}$$

$$(f \oplus g)(x, y) = \max_{(i,j)} \{f(x + i, y + j) - g(i, j)\}$$

Thus, the opening and the closing of  $f$  by  $g$  are respectively the functions

$$f \circ g = (f \ominus g) \oplus g$$

$$f \bullet g = (f \oplus g) \ominus g$$

We define the multiscale function-processing (FP) opening of  $f$  by  $g$  at scale  $n = 0, 1, 2, \dots$  as the function

$$f \circ ng = (f \ominus ng) \oplus ng$$

Likewise, we define the multiscale function-processing (FP) closing of  $f$  by  $g$  as the function

$$f \bullet ng = (f \oplus ng) \ominus ng$$

We can implement multiscale FP opening more efficient as

$$f \circ ng = \left[ \underbrace{(f \ominus g) \ominus g \ominus \dots \ominus g}_{n \text{ times}} \right] \left[ \underbrace{\oplus g \oplus g \oplus \dots \oplus g}_{n \text{ times}} \right]$$

Likewise, for  $f \bullet ng$ . We define the pattern spectrum of  $f$  relative to a discrete graytone pattern  $g$  the function

$$PS_f(n, g) = A[f \circ ng - f \circ (n + 1)g], \quad 0 \leq n \leq N$$

where  $A(f) = \sum_{(x,y)} f(x, y)$  and  $(a - b)(x) = a(x) - b(x)$  denotes the pointwise algebraic difference between functions  $a(x)$  and  $b(x)$ .  $N$  is the maximum positive size  $n$  such that  $f \ominus ng$  is not all  $-\infty$ . A probability density function (pdf) measure is defined as

$$pdf_f(n, B) = \frac{A(PS_x(n, B))}{A(X)}$$

Given the pdf-measure, the cumulative distribution function (cdf) can also be constructed using

$$cdf_f(n, B) = \begin{cases} 0, n = 0 \\ \sum_{r=0}^{n-1} pdf_X(n, B), r + 1 \geq n > 0 \end{cases}$$



## Appendix C. Histogram Features

### C.1. Histogram

The grey level histogram of the ROI of the plaque image is computed for 32 equal width bins and used as a feature set. Histogram despite its simplicity provides a good description of the plaque structure.

### C.2. Multi-region Histogram

Three equidistant ROIs were identified by eroding the plaque image outline by a factor based on the plaque size. The histogram was computed for each one of the three regions as described above and the 96 values comprised the new feature vector. This feature was computed in order to investigate whether the distribution of the plaque structure in equidistant ROIs has a diagnostic value and more specifically if the structure of the outer region of the plaque is critical whether the plaque will rupture or not.

### C.3. Correlogram

Correlograms are histograms, which measure not only statistics about the features of the image, but also consider the spatial distribution of these features. In this work two correlograms were implemented for the ROI of the plaque image:

- based on the distance of the distribution of the pixels' gray level values from the centre of the image, and
- based on their angle of distribution.

For each pixel the distance and the angle from the image centre was calculated and for all pixels with the same distance or angle their histograms were computed. In order to make the comparison between images of different sizes feasible, the distance correlograms were normalized into 32 possible distances from the centre by dividing the calculated distances with  $maximum\_distance/32$ . The angle of the correlogram was allowed to vary among 32 possible values starting from the left middle of the image and moving clockwise. The resulting correlograms were matrices  $32 \times 32$  (gray level values over 32 were set to be the white area surrounding the region of interest and were not consider for the calculation of the features).

## Appendix D. Multi-scale Features

### D.1. Discrete Wavelet Transform (DWT)

The Discrete Wavelet Transform (DWT) of a signal  $x[n]$  is defined as its inner product with a family of functions,  $\phi_{j,k}(t)$  and  $\psi_{j,k}(t)$ , which form an orthonormal set of vectors, a combination of which can completely define the signal, and hence, allow its analysis in many resolution levels  $j$ .

$$\phi_{j,k}(t) = 2^{\frac{j}{2}} \cdot \phi(2^j t - k)$$

$$\psi_{j,k}(t) = 2^{\frac{j}{2}} \cdot \psi(2^j t - k)$$

The functions  $\phi_{j,k}(t)$  and  $\psi_{j,k}(t)$ , consist of versions of the prototype scaling  $\phi(t)$ , and wavelet  $\psi(t)$  functions, discretized at level  $j$  and at translation  $k$ . However, for the implementation of the DWT, only the coefficients of two half-band filters: a low-pass  $h(k)$  and a high-pass  $g(k) = (-1)^k h(1 - k)$  filter, are required, which satisfy the following conditions:

$$\phi_{j+1,0}(t) = \sum_k h[k] \phi_{j,k}$$

$$\psi_{j+1,0}(t) = \sum_k g[k] \psi_{j,k}$$

Hence, the DWT is defined as follows:

$$A_{j+1,n} = \sum_k A_{j,k} \cdot h_j[k - 2n]$$

$$D_{j+1,n} = \sum_k D_{j,k} \cdot g_j[k - 2n]$$

where  $A_{j,n}$  and  $D_{j,n}$  are known as the approximation and detail coefficients, respectively, at level  $j$  and location  $n$ . The outputs  $A_{j,n}$  and  $D_{j,n}$  of the convolution are downsampled by two for every level of analysis, where the time resolution is halved, and the frequency resolution is doubled.

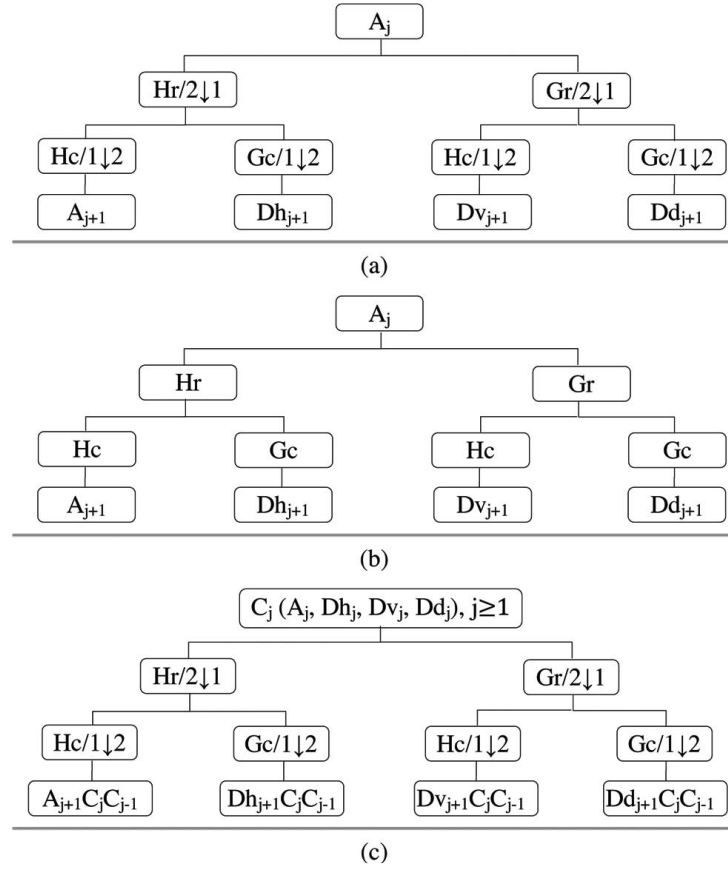


Figure D-1 Schematic diagram of the (a) 2-D DWT, (b) SWT, and (c) WP decomposition schemes for a given level of analysis. Note that, for  $j = 0$ ,  $A_0$  is the original image, whereas for  $j = 1$ ,  $C_0$  is omitted from the abbreviation of WP sub-images.  $Hr$ ,  $Hc$ ,  $Gr$ , and  $Gc$  are the low-pass and high-pass filters on the rows and columns of each sub-image. The symbols “ $2\downarrow 1$ ” and “ $1\downarrow 2$ ” denote the down-sampling procedure on the columns and rows, respectively, which is valid for DWT and WP only (Tsiaparas, et al., 2011).

For images, i.e., 2-D signals, the 2-D DWT can be used. This consists of a DWT on the rows of the image and a DWT on the columns of the resulting image. The result of each DWT is followed by down sampling on the columns and rows, respectively. The decomposition of the image yields four sub-images for every level.

Figure D-1 (a) shows a schematic diagram of the 2-D DWT for a given level of analysis. Each approximation sub-image ( $A_j$ ) is decomposed into four sub images [ $A_{j+1}$ ,  $Dh_{j+1}$ ,  $Dv_{j+1}$  and  $Dd_{j+1}$  named approximation, detail-horizontal, detail-vertical, and detail-diagonal sub-image respectively in Figure D-1 (a)], according to the previously described scheme. Each detail sub-image is the result of a convolution with two half-band filters: a low-pass and a high-pass for  $Dh_j$ , a highpass and a low-pass for  $Dv_j$ , and two high-pass filters for  $Dd_j$  (Tsiaparas, et al., 2011).

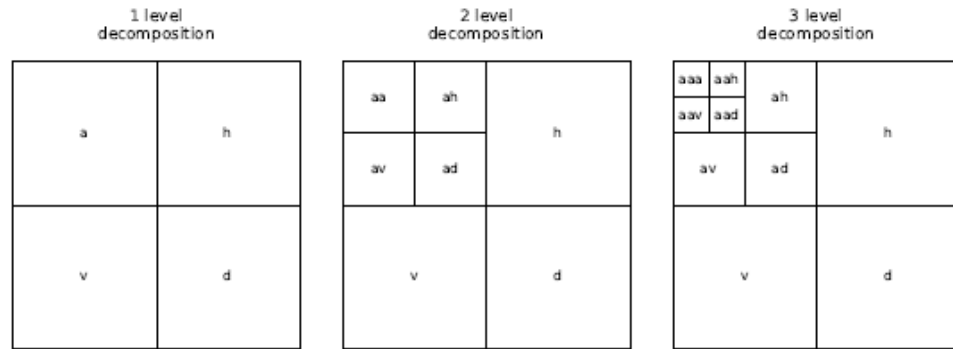


Figure D-2 DWT decomposition (Lee, et al., 2019)

## D.2. Stationary Wavelet Transform (SWT)

The 2-D Stationary Wavelet Transform (SWT) is similar to the 2-D DWT, but no down sampling is performed. Instead, up sampling of the low-pass and high-pass filters is carried out [see Figure D-1 (b)]. The main advantage of SWT over DWT is its shift invariance property. However, it is nonorthogonal and highly redundant, and hence, computationally expensive (Tsiaparas, et al., 2011).

## D.3. Wavelet Packets (WP)

The 2-D Wavelet Packets (WP) decomposition is a simple modification of the 2-D DWT, which offers a richer space-frequency representation. The first level of analysis is the same as that of the 2-D DWT. The second, as well as all subsequent levels of analysis consist of decomposing every sub image, rather than only the approximation sub image, into four new sub images [see Figure D-1 (c)] (Tsiaparas, et al., 2011).

## D.4. Gabor Transform (GT)

The Gabor Transform (GT) of an image consists in convolving that image with the Gabor function, i.e., a sinusoidal plane wave of a certain frequency and orientation modulated by a Gaussian envelope. Frequency and orientation representations of Gabor filters are similar to those of the human visual system, rendering them appropriate for texture segmentation and classification (Tsiaparas, et al., 2011).

## D.5. Selection of Basis Function (DWT, SWT, WP, GT)

Careful selection of the basis function is a critical issue in a wavelet-transform-based methodology for texture analysis. A number of basis functions from different wavelet families were used, including

- Haar (haar)
- Daubechies (db)
- symlets (sym)
- coiflets (coif)
- biorthogonal (bior)

They have compact support but differ in other properties. The Haar wavelet is orthogonal, symmetric, allows for invariant translations, but has poor frequency localization. Daubechies wavelets are orthogonal but not symmetric. Symlets and coiflets are orthogonal and near symmetric. Biorthogonal wavelets combine many of the properties of the other families. They are symmetric with optimum time/frequency localization; however, they are not shift invariant (Tsiaparas, et al., 2011).

#### **D.6. Texture Feature Extraction (DWT, SWT, WP, GT)**

The level of decomposition for each scheme was determined according to the best level of decomposition for WP. The best level algorithm based on an entropy criterion among the complete sub-images was applied, which indicated three levels of decomposition (Tsiaparas, et al., 2011).

The detail sub-images contain the textural information in horizontal, vertical, and diagonal orientations. The approximation sub-images were not used for texture analysis because they are the rough estimate of the original image and capture the intensity variations induced by lighting. The total number of sub-images of three levels of decomposition, including only the detail images, was 9 in the case of DWT and SWT, 63 in the case of WP and 12 in the case of GT. For the GT, the lowest and the highest centre frequencies were set to 0.05 and 0.4, respectively. The size of the Gabor filter used for texture feature extraction was  $13 \times 13$ . Gabor texture information was obtained at 0,45,90,135°.

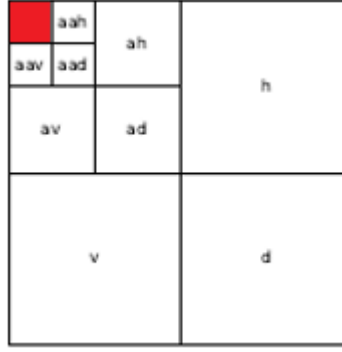


Figure D-3 Multiresolution Feature Extraction: Red sub-image is ignored for analysis (Lee, et al., 2019)

The texture features that were estimated from each detail sub-image were the mean and standard deviation of the absolute value of detail sub-images, both commonly used as texture descriptors:

$$\mu_j = \frac{1}{N_1 \times N_2} \sum_{x=0}^{N_1-1} \sum_{y=0}^{N_2-1} |D_j(x, y)|$$

$$\sigma_j = \frac{1}{N_1 \times N_2} \sum_{x=0}^{N_1-1} \sum_{y=0}^{N_2-1} |D_j(x, y) - \mu_j|^2$$

where  $D_j(x, y)$  are the detail sub-images of dimension  $N_1 \times N_2$  in every orientation at level  $j = 1, 2, 3$ .

### D.7. Amplitude Modulation-Frequency Modulation (AM-FM)

We consider multi-scale Amplitude Modulation – Frequency Modulation (AM-FM) representations, under least-square approximations, for images given by

$$f(x, y) = \sum_{n=0}^{M-1} a_n(x, y) \cdot \cos \varphi_n(x, y)$$

where  $n = 0, 1, \dots, M - 1$  denote different scales,  $a_n(x, y)$  denotes the instantaneous amplitude (IA) for the  $n$ -th AM component, and  $\varphi_n(x, y)$  denotes the instantaneous phase (IP) for the  $n$ -th FM component. In addition, the gradient of the phase  $\nabla \varphi_n(x, y)$  defined as

$$\nabla \varphi_n(x, y) = \begin{bmatrix} \frac{\partial \varphi_n}{\partial x}(x, y) \\ \frac{\partial \varphi_n}{\partial y}(x, y) \end{bmatrix}$$

represents the instantaneous frequency (IF) for the  $n$ -th FM component.

Given the input discrete image  $f(x, y)$ , we first apply the Hilbert transform to form a 2D extension of the 1D analytic signal:  $f_{AS}(x, y)$ .  $f_{AS}(x, y)$  is processed through a collection of bandpass filters with the desired scale. Each processing block will produce the instantaneous amplitude, the instantaneous phase, and the instantaneous frequencies in both  $x$  and  $y$  directions. Figure below depicts the basic AM-FM demodulation method approach.

As feature vector, the histogram of the low, medium, high and dc reconstructed images is used with 32 bins as a probability density function of the image.

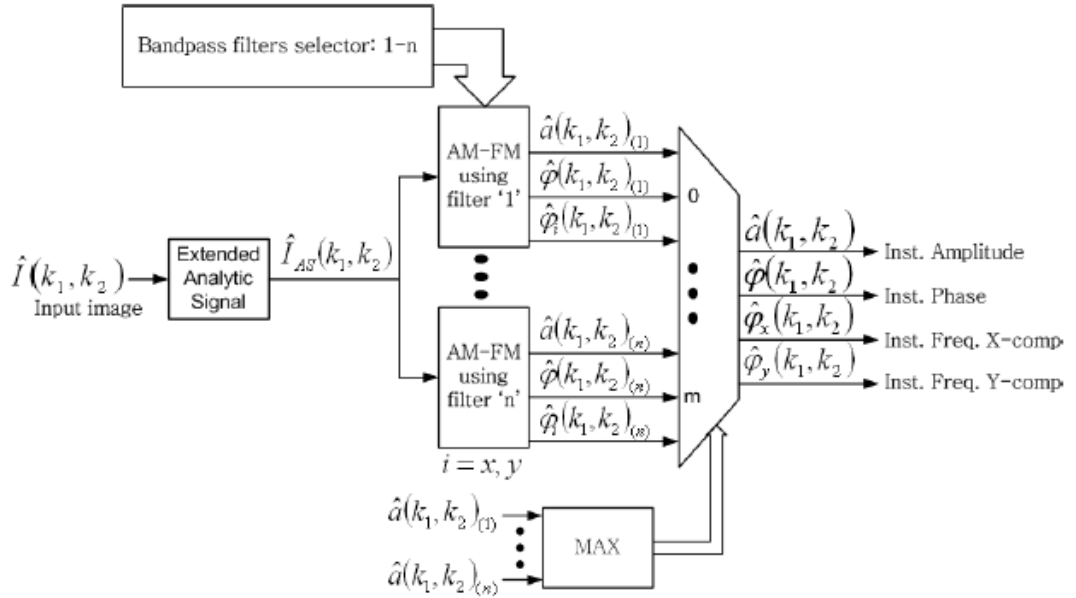


Figure D-4 2-D Multi-scale AM-FM demodulation. Dominant AM-FM components are selected over different image scales. The bandpass filter selector (upper left) is used to define the bandpass filters that correspond to each scale (Murray Herrera, 2009)

## Appendix E. Other Features

### E.1. Image Moments <sup>1</sup>

#### *Raw Moments*

In image processing, computer vision and related fields, an image moment is a certain particular weighted average (moment) of the image pixels' intensities, or a function of such moments, usually chosen to have some attractive property or interpretation.

For a 2-D continuous function  $f(x, y)$  the moment (sometimes called "raw moment") of order  $(p + q)$  is defined as

$$M_{pq} = \int_{-\infty}^{\infty} \int_{-\infty}^{\infty} x^p \cdot y^q \cdot f(x, y) dx dy$$

For  $p, q = 0, 1, 2, \dots$ . For a grayscale image with pixel intensities  $f(x, y)$ , raw image moments  $M_{ij}$  are calculated by

$$M_{ij} = \sum_x \sum_y x^i \cdot y^j \cdot f(x, y)$$

In some cases, this may be calculated by considering the image as a probability density function, i.e., by dividing the above by  $\sum_x \sum_y f(x, y)$

#### *Central Moments*

Central moments are defined as

$$\mu_{pq} = \int_{-\infty}^{\infty} \int_{-\infty}^{\infty} (x - \bar{x})^p \cdot (y - \bar{y})^q \cdot f(x, y) dx dy$$

where  $\bar{x} = \frac{M_{10}}{M_{00}}$  and  $\bar{y} = \frac{M_{01}}{M_{00}}$  are the components of centroid. If  $f(x, y)$  is a digital image, then the previous equation becomes

$$\mu_{pq} = \sum_x \sum_y (x - \bar{x})^p \cdot (y - \bar{y})^q \cdot f(x, y)$$

It can be shown that:

---

<sup>1</sup> [https://en.wikipedia.org/wiki/Image\\_moment](https://en.wikipedia.org/wiki/Image_moment)



$$\mu_{pq} = \sum_m^p \sum_n^q \binom{p}{m} \binom{q}{n} (-\bar{x})^{(p-m)} (-\bar{y})^{(q-n)} M_{mn}$$

### ***Moment Invariants***

Moments are well-known for their application in image analysis since they can be used to derive invariants with respect to specific transformation classes.

The term invariant moments is often abused in this context. However, while moment invariants are invariants that are formed from moments, the only moments that are invariants themselves are the central moments.

Note that the invariants detailed below are exactly invariant only in the continuous domain. In a discrete domain, neither scaling nor rotation are well defined: a discrete image transformed in such a way is generally an approximation, and the transformation is not reversible. These invariants therefore are only approximately invariant when describing a shape in a discrete image.

### ***Translation Invariants***

The central moments  $\mu_{ij}$  of any order are, by construction, invariant with respect to translations.

### ***Scale Invariants***

Invariants  $\eta_{ij}$  with respect to both translation and scale can be constructed from central moments by dividing through a properly scaled zero-th central moment:

$$\eta_{ij} = \frac{\mu_{ij}}{\mu_{00}^{\left(1+\frac{i+j}{2}\right)}}$$

where  $i + j \geq 2$ . Note that translational invariance directly follows by only using central moments.

### ***Rotation Invariants***

See Hu's Moments E.2

## **E.2. Hu's Moments**

As shown by the work of (Hu, 1962), invariants with respect to translation, scale, and rotation can be constructed:

$$I_1 = \eta_{20} + \eta_{02}$$

$$I_2 = (\eta_{20} - \eta_{02})^2 - 4\eta_{11}^2$$

$$I_3 = (\eta_{30} - 3\eta_{12})^2 + (3\eta_{21} - \eta_{03})^2$$

$$I_4 = (\eta_{30} + \eta_{12})^2 + (\eta_{21} + \eta_{03})^2$$

$$I_5 = (\eta_{30} - 3\eta_{12})(\eta_{30} + \eta_{12})[(\eta_{30} + \eta_{12})^2 - 3(\eta_{21} + \eta_{03})^2] \\ + (3\eta_{21} - \eta_{03})(\eta_{21} + \eta_{03})[3(\eta_{30} + \eta_{12})^2 - (\eta_{21} + \eta_{03})^2]$$

$$I_6 = (\eta_{20} - \eta_{02})[(\eta_{30} + \eta_{12})^2 - (\eta_{21} + \eta_{03})^2] + 4\eta_{11}(\eta_{30} + \eta_{12})(\eta_{21} + \eta_{03})$$

$$I_7 = (3\eta_{21} - \eta_{03})(\eta_{30} + \eta_{12})[(\eta_{30} + \eta_{12})^2 - 3(\eta_{21} + \eta_{03})^2] \\ - (\eta_{30} - 3\eta_{12})(\eta_{21} + \eta_{03})[3(\eta_{30} + \eta_{12})^2 - (\eta_{21} + \eta_{03})^2]$$

These are well-known as Hu moment invariants. The first one,  $I_1$ , is analogous to the moment of inertia around the image's centroid, where the pixels' intensities are analogous to physical density. The first six,  $I_1, \dots, I_6$ , are reflection symmetric, i.e., they are unchanged if the image is changed to a mirror image. The last one,  $I_7$ , is reflection antisymmetric (changes sign under reflection), which enables it to distinguish mirror images of otherwise identical images.

### E.3. Zernikes' Moments

Zernikes' moment (Teague, 1980) is a kind of orthogonal complex moments and its kernel is a set of Zernike complete orthogonal polynomials defined over the interior of the unit disc in the polar coordinates space. Let  $f(r, \theta)$  be the image intensity function, and the 2-D Zernike moment of order  $m$  with repetition  $n$  is defined as:

$$Z_{mn} = \frac{m+1}{\pi} \int_0^{2\pi} \int_0^1 f(r, \theta) \cdot V_{mn}^*(r, \theta) \cdot r \, dr d\theta, r \leq 1$$

where  $V_{mn}^*(r, \theta)$  is the complex conjugate of Zernike polynomial  $V_{mn}(r, \theta)$  and  $m$  and  $n$  both are integer and the relation between  $m$  and  $n$  can be described as:

$$V_{mn}(r, \theta) = R_{mn}(r) \cdot e^{j \cdot n \cdot \theta}$$

where  $j = \sqrt{-1}$  and the orthogonal radial polynomial  $R_{mn}(r)$  is given by

$$R_{mn}(r) = \sum_{s=0}^{\frac{m-|n|}{2}} (-1)^s \cdot \frac{(m-s)!}{s! \cdot \left(\frac{m+|n|}{2} - s\right)! \cdot \left(\frac{m-|n|}{2} - s\right)!} \cdot r^{m-2 \cdot s}$$

From the formula mentioned above and the Euler's complex number formula, the equations listed as follows are available.

$$R_{m(-n)}(r) = R_{mn}(r)$$

$$V_{mn}^*(r, \theta) = V_{m(-n)}(r, \theta)$$

For the computer digital image, let  $f(r, \theta)$  be the intensity of the image pixel, and the 2-D Zernike moment can be represented as:

$$Z_{mn} = \frac{m+1}{\pi} \sum_r \sum_{\theta} f(r, \theta) \cdot V_{mn}^*(r, \theta)$$

(Liu, He, & Ye, 2007)

# Bibliography

---

- Acharya U. R., Chua, C. K., Ng, E. Y., Yu, W., & Chee, C. (2008, 12 01). Application of Higher Order Spectra for the Identification of Diabetes Retinopathy Stages. *Journal of Medical Systems*, 32, 481-488. doi:10.1007/s10916-008-9154-8
- Acharya, U. R., Chua, K., Lim, T.-C., Tay, D., & Suri, J. (2009, 12). Automatic identification of epileptic EEG signals using nonlinear parameters. *Journal of Mechanics in Medicine and Biology*, 9, 539-553. doi:10.1142/S0219519409003152
- Acharya, U. R., Faust, O., Alvin, A., Subbhuraam, V. S., Molinari, F., Saba, L., . . . Suri, J. (2011, 6). Symptomatic vs. Asymptomatic Plaque Classification in Carotid Ultrasound. *Journal of medical systems*, 36, 1861-71. doi:10.1007/s10916-010-9645-2
- Acharya, U. R., Faust, O., Sree, S. V., Alvin, A. P., Krishnamurthi, G., Seabra, J. C., . . . Suri, J. S. (2011, 8). AtheromaticTM: Symptomatic vs. asymptomatic classification of carotid ultrasound plaque using a combination of HOS, DWT & texture. *2011 Annual International Conference of the IEEE Engineering in Medicine and Biology Society*. IEEE. doi:10.1109/iembs.2011.6091113
- Acharya, U. R., Faust, O., Sree, S. V., Molinari, F., Saba, L., Nicolaides, A., & Suri, J. S. (2012). An Accurate and Generalized Approach to Plaque Characterization in 346 Carotid Ultrasound Scans. *IEEE Transactions on Instrumentation and Measurement*, 61, 1045-1053. doi:10.1109/TIM.2011.2174897
- Acharya, U. R., Mookiah, M. R., Sree, S. V., Afonso, D., Sanches, J., Shafique, S., . . . Suri, J. S. (2013, 1). Atherosclerotic plaque tissue characterization in 2D ultrasound longitudinal carotid scans for automated classification: a paradigm for stroke risk assessment. *Medical & Biological Engineering & Computing*, 51, 513–523. doi:10.1007/s11517-012-1019-0
- Acharya, U. R., Subbhuraam, V. S., Molinari, F., Saba, L., Nicolaides, A., Shafique, S., & Suri, J. (2012, 8). Carotid ultrasound symptomatology using atherosclerotic plaque characterization: A class of Atheromatic systems., *2012*, pp. 3199-202. doi:10.1109/EMBC.2012.6346645
- Acharya, U. R., Subbhuraam, V. S., Mookiah, M. R., Molinari, F., Saba, L., Ho, S., . . . Suri, J. (2012, 4). Atherosclerotic Risk Stratification Strategy for Carotid Arteries Using Texture-Based Features. *Ultrasound in Medicine & Biology*, 38, 899-915. doi:10.1016/j.ultrasmedbio.2012.01.015
- Amadasun, M., & King, R. (1989). Textural features corresponding to textural properties. *IEEE Trans. Syst. Man Cybern.*, 19, 1264-1274.
- Ariyoshi, K., Okuya, S., Kunitsugu, I., Matsunaga, K., Nagao, Y., Nomiyama, R., . . . Tanizawa, Y. (2014, 6). Ultrasound analysis of gray-scale median value of carotid plaques is a useful reference index for cerebro-cardiovascular events in patients with type 2 diabetes. *Journal of Diabetes Investigation*, 6, 91–97. doi:10.1111/jdi.12242
- Asvestas, P. A., Golemati, S., Matsopoulos, G. K., Nikita, K. S., & Nicolaides, A. N. (2002). Fractal Dimension Estimation of Carotid Atherosclerotic Plaques from B-mode Ultrasound: A Pilot Study. *Ultrasound in Medicine and Biology*, 28, 1129-1136.

- Biasi, G. M., Mingazzini, P. M., Baronio, L., Piglionica, M. R., Ferrari, S. A., Elatrozy, T. S., & Nicolaides, A. N. (1998, 8). Carotid Plaque Characterization Using Digital Image Processing and its Potential in Future Studies of Carotid Endarterectomy and Angioplasty. *Journal of Endovascular Therapy*, 5, 240–246. doi:10.1177/152660289800500309
- Biasi, G., Frolo, A., Diethrich, E., Deleo, G., Galimberti, S., Mingazzini, P., . . . Valsecchi, M. (2004, 9). Carotid Plaque Echolucency Increases the Risk of Stroke in Carotid Stenting The Imaging in Carotid Angioplasty and Risk of Stroke (ICAROS) Study. *Circulation*, 110, 756-62. doi:10.1161/01.CIR.0000138103.91187.E3
- Bottou, L. (2010, 1). Large-Scale Machine Learning with Stochastic Gradient Descent. *Proc. of COMPSTAT*. doi:10.1007/978-3-7908-2604-3\_16
- Chen, T., Kornblith, S., Norouzi, M., & Hinton, G. (2020). A Simple Framework for Contrastive Learning of Visual Representations. *A Simple Framework for Contrastive Learning of Visual Representations*.
- Christodoulou, C. I., Pattichis, C. S., Murray, V., Pattichis, M. S., & Nicolaides, A. (2009). AM-FM Representations for the Characterization of Carotid Plaque Ultrasound Images. In *IFMBE Proceedings* (pp. 546–549). Springer Berlin Heidelberg. doi:10.1007/978-3-540-89208-3\_130
- Christodoulou, C., Kyriacou, E., Pattichis, C., & Nicolaides, A. (2006, 10). Multiple Feature Extraction for Content-Based Image Retrieval of Carotid Plaque Ultrasound Images.
- Christodoulou, C., Kyriacou, E., Pattichis, M., Pattichis, C., & Nicolaides, A. (2003, 8). A Comparative Study of Morphological and Other Texture Features for the Characterization of Atherosclerotic Carotid Plaques., 2756, pp. 503-511. doi:10.1007/978-3-540-45179-2\_62
- Christodoulou, C., Loizou, C., Pattichis, C., Pantzaris, M., Kyriacou, E., Pattichis, M., . . . Nicolaides, A. (2002, 2). De-speckle filtering in ultrasound imaging of the carotid artery., 2, pp. 1027 - 1028 vol.2. doi:10.1109/IEMBS.2002.1106259
- Christodoulou, C., Pattichis, C., Pantzaris, M., & Nicolaides, A. (2003, 8). Texture Based Classification of Atherosclerotic Carotid Plaques. *IEEE transactions on medical imaging*, 22, 902-12. doi:10.1109/TMI.2003.815066
- Christodoulou, C., Pattichis, C., Pantzaris, M., Tegos, T., Nicolaides, A., Elatrozy, T., . . . Dhanjil, S. (1999, 2). Multi-feature texture analysis for the classification of carotid plaques., 5, pp. 3591 - 3596 vol.5. doi:10.1109/IJCNN.1999.836249
- Chua, K., Chandran, V., Acharya, U. R., & Lim, C. (2009, 6). Automatic identification of epileptic electroencephalography signals using higher-order spectra. *Proceedings of the Institution of Mechanical Engineers. Part H, Journal of engineering in medicine*, 223, 485-95. doi:10.1243/09544119JEIM484
- Chua, K., Chandran, V., Acharya, U. R., & Lim, C. (2011, 12). Application of Higher Order Spectra to Identify Epileptic EEG. *Journal of medical systems*, 35, 1563-71. doi:10.1007/s10916-010-9433-z
- Constantinou, K. P., Constantinou, I. P., Pattichis, C. S., & Pattichis, M. S. (2021). Medical Image Analysis Using AM-FM Models and Methods. *IEEE Reviews in Biomedical Engineering*, 14, 270-289. doi:10.1109/RBME.2020.2967273
- Elatrozy, T., Nicolaides, A., Tegos, T., & Griffin, M. (1998, 9). The objective characterisation of ultrasonic carotid plaque features. *European Journal of Vascular and Endovascular Surgery*, 16, 223–230. doi:10.1016/s1078-5884(98)80224-4

- El-Barghouty, N., Geroulakos, G., Nicolaides, A., Androulakis, A., & Bahal, V. (1995, 5). Computer-assisted carotid plaque characterisation. *European Journal of Vascular and Endovascular Surgery*, 9, 389–393. doi:10.1016/s1078-5884(05)80005-x
- Fujii, K., Sugi, S., & Ando, Y. (2003, 9). Textural properties corresponding to visual perception based on the correlation mechanism in the visual system. *Psychological research*, 67, 197-208. doi:10.1007/s00426-002-0113-6
- Fukushima, K. (1980, 4). Neocognitron: A self-organizing neural network model for a mechanism of pattern recognition unaffected by shift in position. *Biological Cybernetics*, 36, 193–202. doi:10.1007/bf00344251
- Galloway, M. M. (1975). Texture analysis using gray level run lengths. *Computer Graphics and Image Processing*, 4, 172-179. doi:https://doi.org/10.1016/S0146-664X(75)80008-6
- Geroulakos, G., Domjan, J., Nicolaides, A., Stevens, J., Labropoulos, N., Ramaswami, G., . . . Mansfield, A. (1994, 8). Ultrasonic carotid artery plaque structure and the risk of cerebral infarction on computed tomography. *Journal of Vascular Surgery*, 20, 263–266. doi:10.1016/0741-5214(94)90014-0
- Goodfellow, I., Bengio, Y., & Courville, A. (2016). *Deep Learning*. MIT Press.
- Griffin, M. B., Kyriacou, E., Pattichis, C., Bond, D., Kakkos, S. K., Sabetai, M., . . . Nicolaides, A. (2010). Juxtaluminal hypoechoic area in ultrasonic images of carotid plaques and hemispheric symptoms. *Journal of Vascular Surgery*, 52, 69-76. doi:https://doi.org/10.1016/j.jvs.2010.02.265
- Griffin, M., Nicolaides, A., & Kyriacou, E. (2008, 1). Normalisation of ultrasonic images of atherosclerotic plaques and reproducibility of grey scale median using dedicated software. *International angiology : a journal of the International Union of Angiology*, 26, 372-7.
- Hamilton, N., Pantelic, R., Hanson, K., & Teasdale, R. (2007, 3). Fast automated cell phenotype classification. *BMC bioinformatics*, 8, 110. doi:10.1186/1471-2105-8-110
- Haralick, R., Shanmugam, K., & Dinstein, I. (1973, 1). Textural Features for Image Classification. *IEEE Trans Syst Man Cybern, SMC-3*, 610-621.
- Hotelling, H. (1933). Analysis of a complex of statistical variables into principal components. *Journal of Educational Psychology*, 24, 417–441. doi:10.1037/h0071325
- [https://en.wikipedia.org/wiki/Feature\\_scaling](https://en.wikipedia.org/wiki/Feature_scaling). (n.d.).
- Hu, M. (1962). Visual pattern recognition by moment invariants. *IRE Trans. Inf. Theory*, 8, 179-187.
- Hubel, D. H., & Wiesel, T. N. (1968). Receptive fields and functional architecture of monkey striate cortex. *The Journal of Physiology*, 195, 215-243. doi:https://doi.org/10.1113/jphysiol.1968.sp008455
- Iannuzzi, A., Wilcosky, T., Mercuri, M., Rubba, P., Bryan, F. A., & Bond, M. G. (1995, 4). Ultrasonographic Correlates of Carotid Atherosclerosis in Transient Ischemic Attack and Stroke. *Stroke*, 26, 614–619. doi:10.1161/01.str.26.4.614
- Ioffe, S., & Szegedy, C. (2015). Batch Normalization: Accelerating Deep Network Training by Reducing Internal Covariate Shift. *Batch Normalization: Accelerating Deep Network Training by Reducing Internal Covariate Shift*.
- Johri, A. M., Nambi, V., Naqvi, T. Z., Feinstein, S. B., Kim, E. S., Park, M. M., . . . Sillesen, H. (2020). Recommendations for the Assessment of Carotid Arterial Plaque by Ultrasound for the Characterization of Atherosclerosis and Evaluation of Cardiovascular Risk: From the American Society of

- Echocardiography. *Journal of the American Society of Echocardiography*, 33, 917-933. doi:<https://doi.org/10.1016/j.echo.2020.04.021>
- Kakkos, S. K., Nicolaides, A. N., Kyriacou, E., Daskalopoulou, S. S., Sabetai, M. M., Pattichis, C. S., . . . Thomas, D. (2011, 4). Computerized Texture Analysis of Carotid Plaque Ultrasonic Images Can Identify Unstable Plaques Associated With Ipsilateral Neurological Symptoms. *Angiology*, 62, 317–328. doi:10.1177/0003319710384397
- Kakkos, S. K., Stevens, J. M., Nicolaides, A. N., Kyriacou, E., Pattichis, C. S., Geroulakos, G., & Thomas, D. (2007, 4). Texture Analysis of Ultrasonic Images of Symptomatic Carotid Plaques can Identify Those Plaques Associated with Ipsilateral Embolic Brain Infarction. *European Journal of Vascular and Endovascular Surgery*, 33, 422–429. doi:10.1016/j.ejvs.2006.10.018
- Khosla, P., Teterwak, P., Wang, C., Sarna, A., Tian, Y., Isola, P., . . . Krishnan, D. (2021). Supervised Contrastive Learning. *Supervised Contrastive Learning*.
- Kingma, D. P., & Ba, J. (2015). Adam: A Method for Stochastic Optimization. *CoRR*, abs/1412.6980.
- Krizhevsky, A., Sutskever, I., & Hinton, G. E. (2012). ImageNet Classification with Deep Convolutional Neural Networks. In F. Pereira, C. J. Burges, L. Bottou, & K. Q. Weinberger (Eds.), *Advances in Neural Information Processing Systems 25* (pp. 1097–1105). Curran Associates, Inc. Retrieved from <http://papers.nips.cc/paper/4824-imagenet-classification-with-deep-convolutional-neural-networks.pdf>
- Kyriacou, E., Pattichis, C., Karaolis, M., Loizou, C., Christodoulou, C., Pattichis, M., . . . Nicolaides, A. (2007, 9). An Integrated System for Assessing Stroke Risk. *IEEE engineering in medicine and biology magazine : the quarterly magazine of the Engineering in Medicine & Biology Society*, 26, 43-50. doi:10.1109/EMB.2007.901794
- Kyriacou, E., Pattichis, C., Pattichis, M., Mavrommatis, A., Panayiotou, S., Christodoulou, C., . . . Nicolaides, A. (2006, 6). Classification of Atherosclerotic Carotid Plaques Using Gray Level Morphological Analysis on Ultrasound images., 204, pp. 737-744. doi:10.1007/0-387-34224-9\_87
- Kyriacou, E., Pattichis, M., Christodoulou, C., Pattichis, C., Kakkos, S., & Nicolaides, A. (2005, 9). Multiscale Morphological Analysis of the Atherosclerotic Carotid Plaque., 2, pp. 1626-9. doi:10.1109/IEMBS.2005.1616750
- Kyriacou, E., Pattichis, M., Christodoulou, C., Pattichis, C., Kakkos, S., Griffin, M., & Nicolaides, A. (2005, 2). Ultrasound imaging in the analysis of carotid plaque morphology for the assessment of stroke.
- Kyriacou, E., Pattichis, M., Pattichis, C., Mavrommatis, A., Christodoulou, C., Kakkos, S., & Nicolaides, A. (2009, 2). Classification of atherosclerotic carotid plaques using morphological analysis on ultrasound images. *Applied Intelligence*, 30, 3-23. doi:10.1007/s10489-007-0072-0
- Kyriacou, E., Petroudi, S., Pattichis, C., Pattichis, M., Griffin, M., Kakkos, S., & Nicolaides, A. (2012, 4). Prediction of High-Risk Asymptomatic Carotid Plaques Based on Ultrasonic Image Features. *IEEE transactions on information technology in biomedicine : a publication of the IEEE Engineering in Medicine and Biology Society*, 16, 966-73. doi:10.1109/TITB.2012.2192446
- Laws, K. (1980). Rapid texture identification.

- Lecun, Y., Bottou, L., Bengio, Y., & Haffner, P. (1998). Gradient-based learning applied to document recognition. *Proceedings of the IEEE*, 86, 2278-2324. doi:10.1109/5.726791
- Lee, G. R., Gommers, R., Waselewski, F., Wohlfahrt, K., O&#217, & Leary. (2019). PyWavelets: A Python package for wavelet analysis. *Journal of Open Source Software*, 4, 1237. doi:10.21105/joss.01237
- Liu, M., He, Y., & Ye, B. (2007). Image Zernike moments shape feature evaluation based on image reconstruction. *Geo-spatial Information Science*, 10, 191-195. doi:10.1007/s11806-007-0060-x
- Loizou, C. (2008, 5). Despeckle filtering in ultrasound imaging of the carotid artery.
- Loizou, C., Murray, V., Pattichis, M., Christodoulou, C., Pantzaris, M., Nicolaides, A., & Pattichis, C. (2009, 9). AM-FM Texture Image Analysis of the Intima and Media Layers of the Carotid Artery., 5769, pp. 885-894. doi:10.1007/978-3-642-04277-5\_89
- Mandelbrot, B. (1977). Fractal Geometry of Nature.
- Maragos, P. (1989, 8). Pattern spectrum and multiscale shape representation. *IEEE Trans Pattern Anal Mach Intell. Pattern Analysis and Machine Intelligence, IEEE Transactions on*, 11, 701-716. doi:10.1109/34.192465
- Maragos, P., & Ziff, R. (1990, 6). Threshold Superposition in Morphological Image Analysis Systems. *Pattern Analysis and Machine Intelligence, IEEE Transactions on*, 12, 498-504. doi:10.1109/34.55110
- Mougiakakou, S., Golemati, S., Gousias, I., Nicolaides, A., & Nikita, K. (2007, 2). Computer-aided Diagnosis of Carotid Atherosclerosis based on Ultrasound Image Statistics, Laws' texture and Neural networks. *Ultrasound in medicine & biology*, 33, 26-36. doi:10.1016/j.ultrasmedbio.2006.07.032
- Murray Herrera, V. M. (2009). *AM-FM methods for image and video processing*. Retrieved from <https://digitalrepository.unm.edu/>
- Murray, V., Murillo, S., Pattichis, M., Loizou, C., Pattichis, C., Kyriacou, E., & Nicolaides, A. (2007, 12). An AM-FM model for Motion Estimation in Atherosclerotic Plaque Videos., (pp. 746-750). doi:10.1109/ACSSC.2007.4487315
- Murray, V., Rodriguez, P., & Pattichis, M. (2010, 6). Multiscale AM-FM Demodulation and Image Reconstruction Methods With Improved Accuracy. *Image Processing, IEEE Transactions on*, 19, 1138-1152. doi:10.1109/TIP.2010.2040446
- Nair, V., & Hinton, G. E. (2010). Rectified Linear Units Improve Restricted Boltzmann Machines. *Proceedings of the 27th International Conference on International Conference on Machine Learning* (pp. 807-814). Madison: Omnipress.
- Ng, A. Y. (2004). Feature Selection,  $L_1$  vs.  $L_2$  Regularization, and Rotational Invariance. *Proceedings of the Twenty-First International Conference on Machine Learning* (p. 78). New York, NY, USA: Association for Computing Machinery. doi:10.1145/1015330.1015435
- Ojala, T., Pietikäinen, M., & Harwood, D. (1996). A comparative study of texture measures with classification based on featured distributions. *Pattern Recognition*, 29, 51-59. doi:[https://doi.org/10.1016/0031-3203\(95\)00067-4](https://doi.org/10.1016/0031-3203(95)00067-4)
- Ojala, T., Pietikäinen, M., & Harwood, D. (1996). A comparative study of texture measures with classification based on featured distributions. *Pattern Recognit.*, 29, 51-59.



- Ojala, T., Pietikäinen, M., & Maenpää, T. (2002, 8). Multiresolution Gray-Scale and Rotation Invariant Texture Classification with Local Binary Patterns. *Pattern Analysis and Machine Intelligence, IEEE Transactions on*, 24, 971-987. doi:10.1109/TPAMI.2002.1017623
- Pattichis, C., Christodoulou, C., Kyriacou, E., & Nicolaides, A. (2010, 1). Image Retrieval and Classification of Carotid Plaque Ultrasound Images. *Image Retrieval and Classification of Carotid Plaque Ultrasound Images*, 2, 18-28.
- Pearson, K. (1901). LIII. On lines and planes of closest fit to systems of points in space. *The London, Edinburgh, and Dublin Philosophical Magazine and Journal of Science*, 2, 559-572. doi:10.1080/14786440109462720
- Peng, H., Long, F., & Ding, C. (2005). Feature selection based on mutual information criteria of max-dependency, max-relevance, and min-redundancy. *IEEE Transactions on Pattern Analysis and Machine Intelligence*, 27, 1226-1238. doi:10.1109/TPAMI.2005.159
- Polak, J. F., Shemanski, L., O'textquotesingleLeary, D. H., Lefkowitz, D., Price, T. R., Savage, P. J., . . . Reid, C. (1998, 9). Hypoechoic plaque at US of the carotid artery: an independent risk factor for incident stroke in adults aged 65 years or older. Cardiovascular Health Study. *Radiology*, 208, 649-654. doi:10.1148/radiology.208.3.9722841
- Prahl, U., Holdfeldt, P., Bergström, G., Fagerberg, B., Hulthe, J., & Gustavsson, T. (2009, 12). Percentage White: A New Feature for Ultrasound Classification of Plaque Echogenicity in Carotid Artery Atherosclerosis. *Ultrasound in medicine & biology*, 36, 218-26. doi:10.1016/j.ultrasmedbio.2009.10.002
- Rakebrandt, F., Crawford, D. C., Havard, D., Coleman, D., & Woodcock, J. P. (2000). Relationship between ultrasound texture classification images and histology of atherosclerotic plaque. *Ultrasound in Medicine & Biology*, 26, 1393-1402. doi:https://doi.org/10.1016/S0301-5629(00)00314-8
- Ruder, S. (2016). An overview of gradient descent optimization algorithms. *CoRR*, abs/1609.04747. Retrieved from <http://arxiv.org/abs/1609.04747>
- Rumelhart, D. E., Hinton, G. E., & Williams, R. J. (1986). Learning Internal Representations by Error Propagation. In *Parallel Distributed Processing: Explorations in the Microstructure of Cognition, Vol. 1: Foundations* (pp. 318-362). Cambridge, MA, USA: MIT Press.
- Russakovsky, O., Deng, J., Su, H., Krause, J., Satheesh, S., Ma, S., . . . Li, F.-F. (2014). ImageNet Large Scale Visual Recognition Challenge. *CoRR*, abs/1409.0575. Retrieved from <http://arxiv.org/abs/1409.0575>
- Saba, L., Sanagala, S. S., Gupta, S., Koppula, V., Johri, A., Sharma, A., . . . Suri, J. (2021, 5). Ultrasound-based internal carotid artery plaque characterization using deep learning paradigm on a supercomputer: a cardiovascular disease/stroke risk assessment system. *The International Journal of Cardiovascular Imaging*, 37. doi:10.1007/s10554-020-02124-9
- Skandha, S. S., Gupta, S. K., Saba, L., Koppula, V. K., Johri, A. M., Khanna, N. N., . . . Suri, J. S. (2020, 10). 3-D optimized classification and characterization artificial intelligence paradigm for cardiovascular/stroke risk stratification using carotid ultrasound-based delineated plaque: Atheromatic™ 2.0. *Computers in Biology and Medicine*, 125, 103958. doi:10.1016/j.compbiomed.2020.103958
- Srivastava, N., Hinton, G., Krizhevsky, A., Sutskever, I., & Salakhutdinov, R. (2014). Dropout: A Simple Way to Prevent Neural Networks from Overfitting. *Journal*

- of *Machine Learning Research*, 15, 1929-1958. Retrieved from <http://jmlr.org/papers/v15/srivastava14a.html>
- Sultana, F., Sufian, A., & Dutta, P. (2019). Advancements in Image Classification using Convolutional Neural Network. *CoRR*, *abs/1905.03288*. Retrieved from <http://arxiv.org/abs/1905.03288>
- Sultana, F., Sufian, A., & Dutta, P. (2020). A Review of Object Detection Models Based on Convolutional Neural Network. *Intelligent Computing: Image Processing Based Applications*, 1–16. doi:10.1007/978-981-15-4288-6\_1
- Sztajzel, R., Momjian, S., Isabelle, M., Murith, N., Djebaili, K., Boissard, G., . . . Pizolatto, G. (2005, 5). Stratified Gray-Scale Median Analysis and Color Mapping of the Carotid Plaque: Correlation With Endarterectomy Specimen Histology of 28 Patients. *Stroke; a journal of cerebral circulation*, 36, 741-5. doi:10.1161/01.STR.0000157599.10026.ad
- Tang, X. (1998, 12). Texture information in run-length matrices. *Image Processing, IEEE Transactions on*, 7, 1602-1609. doi:10.1109/83.725367
- Teague, M. R. (1980, 8). Image analysis via the general theory of moments\*. *J. Opt. Soc. Am.*, 70, 920–930. doi:10.1364/JOSA.70.000920
- Tegos, T. J., Mavrophoros, D., Sabetai, M. M., Elatrozy, T. S., Dhanjil, S., Karapataki, M., . . . Nicolaides, A. N. (2001). Types of neurovascular symptoms and carotid plaque ultrasonic textural characteristics. *Journal of Ultrasound in Medicine*, 20, 113-121. doi:<https://doi.org/10.7863/jum.2001.20.2.113>
- Tegos, T., Sohail, M., Sabetai, M., Robless, P., Akbar, N., Pare, G., . . . Nicolaides, A. (2000, 11). Echomorphologic and histopathologic characteristics of unstable carotid plaques. *AJNR. American journal of neuroradiology*, 21, 1937-44.
- Thibault, G., Fertil, B., Navarro, C., Pereira, S., Cau, P., Lévy, N., . . . Mari, J. (2009). Texture indexes and gray level size zone matrix. Application to cell nuclei classification.
- Toet, A. (1990). A hierarchical morphological image decomposition. *Pattern Recognition Letters*, 11, 267-274. doi:[https://doi.org/10.1016/0167-8655\(90\)90065-A](https://doi.org/10.1016/0167-8655(90)90065-A)
- Tsiaparas, N., Golemati, S., Andreadis, I., Stoitsis, J. S., Valavanis, I., & Nikita, K. S. (2011, 1). Comparison of Multiresolution Features for Texture Classification of Carotid Atherosclerosis From B-Mode Ultrasound. *IEEE Transactions on Information Technology in Biomedicine*, 15, 130–137. doi:10.1109/titb.2010.2091511
- Weszka, J. S., Dyer, C. R., & Rosenfeld, A. (1976). A Comparative Study of Texture Measures for Terrain Classification. *IEEE Transactions on Systems, Man, and Cybernetics*, *SMC-6*, 269-285. doi:10.1109/TSMC.1976.5408777
- wikipedia. (n.d.). Retrieved from [https://en.wikipedia.org/wiki/Image\\_moment](https://en.wikipedia.org/wiki/Image_moment)
- Wilhjelm, J., Grønholdt, M., Wiebe, B., Jespersen, S. K., Hansen, L. K., & Sillesen, H. (1998). Quantitative analysis of ultrasound B-mode images of carotid atherosclerotic plaque: correlation with visual classification and histological examination. *IEEE Transactions on Medical Imaging*, 17, 910-922.
- Wu, C.-M., & Chen, Y.-C. (1992). Statistical feature matrix for texture analysis. *CVGIP: Graphical Models and Image Processing*, 54, 407-419. doi:[https://doi.org/10.1016/1049-9652\(92\)90025-S](https://doi.org/10.1016/1049-9652(92)90025-S)
- Wu, C.-M., Chen, Y.-C., & Hsieh, K.-S. (1992). Texture features for classification of ultrasonic liver images. *IEEE Transactions on Medical Imaging*, 11, 141-152. doi:10.1109/42.141636

- Wu, Z., Huang, N., & Chen, X. (2009, 7). The Multi-Dimensional Ensemble Empirical Mode Decomposition Method. *Advances in Adaptive Data Analysis, 1*, 339-372. doi:10.1142/S1793536909000187
- Zaitoun, N. M., & Aqel, M. J. (2015). Survey on Image Segmentation Techniques. *Procedia Computer Science*, 65, 797-806. doi:https://doi.org/10.1016/j.procs.2015.09.027